

# Variable Eddington Factor Method for $S_N$ Equations with Discontinuous Galerkin Spatial Discretization and a Mixed Finite-Element Balance Equation

Samuel S. Olivier, Jim E. Morel

Department of Nuclear Engineering  
Texas A&M University  
College Station, TX 77843

## Abstract

*We present the Variable Eddington Factor (VEF) method, a non-linear Discrete Ordinates Source Iteration scheme that relaxes the consistency requirement of the transport and acceleration steps' spatial discretization. The method was applied to the 1-D, one-group neutron transport equation with Lumped Linear Discontinuous Galerkin (LLDG) transport and the constant-linear Mixed Finite Element Method (MFEM) drift diffusion acceleration. Methods for increased consistency between the transport and acceleration steps are also presented. The VEF method exhibited second-order convergence as expected from the orders of accuracy of LLDG and MFEM in isolation, accelerated source iterations as well as consistently differenced  $S_2SA$ , and survived the thick diffusion limit. In addition, the difference between the transport and acceleration steps' solution was shown to converge as the mesh was refined.*

## Keywords

Variable Eddington Factor, Source Iteration Acceleration, Lumped Linear Discontinuous Galerkin, Mixed Finite Element Method

## Running Head

Variable Eddington Factor Method

## Corresponding Author

Jim E. Morel, email: [morel@tamu.edu](mailto:morel@tamu.edu).

# 1 Introduction

The Variable Eddington Factor (VEF) method, also known as Quasi-Diffusion (QD), was one of the first nonlinear methods for accelerating source iterations in  $S_N$  calculations [1]. It is comparable in effectiveness to both linear and nonlinear forms of Diffusion-Synthetic Acceleration (DSA), but it offers much more flexibility than the DSA. Stability can only be guaranteed with DSA if the diffusion equation is differenced in a manner consistent with that of the  $S_N$  equations [2]. Modern  $S_N$  codes often use advanced discretization schemes such as discontinuous Galerkin (DG) since classic discretization schemes such as step and diamond are not suitable for radiative transfer calculations in the High Energy Density Laboratory Physics (HEDLP) regime or coupled electron-photon calculations. Diffusion discretizations consistent with DG  $S_N$  discretizations cannot actually be expressed in diffusion form, but rather must be expressed in first-order or  $P_1$  form, and are much more difficult to solve than standard diffusion discretizations [3]. Considerable effort has gone into the development of “partially consistent” diffusion discretizations that yield a stable DSA algorithm with some degree of degraded effectiveness, but such discretizations are also generally difficult to develop [4, 5, 6]. A great advantage of the VEF method is that the drift-diffusion equation that accelerates the  $S_N$  source iterations can be discretized in any valid manner without concern for consistency with the  $S_N$  discretization. When the VEF drift-diffusion equation is discretized in a way that is “non-consistent,” the  $S_N$  and VEF drift-diffusion solutions for the scalar flux do not necessarily become identical when the iterative process converges. However, they do become identical in the limit as the spatial mesh is refined, and the difference between the two solutions is proportional to the spatial truncation errors associated with the  $S_N$  and drift-diffusion discretizations. In general the order accuracy of the  $S_N$  and VEF drift-diffusion solutions will be the lowest order accuracy of their respective indepen-

dent discretizations. Although the  $S_N$  solution obtained with such a “non-consistent” VEF method is not conservative, the VEF drift-diffusion solution is in fact conservative. This is particularly useful in multiphysics calculations where the low-order VEF equation can be coupled to the other physics components rather than the high-order  $S_N$  equations. Another advantage of the non-consistent approach is that even if the  $S_N$  spatial discretization scheme does not preserve the thick diffusion limit [7], that limit will generally be preserved using the VEF method.

The purpose of this paper is to investigate the application of the VEF method with the 1-D  $S_N$  equations discretized with the lumped linear-discontinuous method (LLDG) and the drift-diffusion equation discretized using the constant-linear mixed finite-element method (MFEM). To our knowledge, this combination has not been previously investigated. Our motivation for this investigation is that MFEM methods are now being used for high-order hydrodynamics calculations [8]. A radiation transport method compatible with MFEM methods is clearly desirable for developing a MFEM radiation-hydrodynamics code. Such a code would combine thermal radiation transport with hydrodynamics. However, MFEM methods are inappropriate for the standard first-order form of the transport equation. Thus the use of the VEF method with a DG  $S_N$  discretization and a MFEM drift-diffusion discretization suggests itself. Here we define a VEF method that should exhibit second-order accuracy since both the transport and drift-diffusion discretizations are second-order accurate in isolation. In addition, our VEF method should preserve the thick diffusion limit, which is essential for radiative transfer calculations in the HEDLP regime. We use the lumped rather than the standard Linear Discontinuous Galerkin discretization because lumping yields a much more robust scheme, and robustness is essential for radiative transfer calculations in the HEDLP regime. Because this is an initial study, we simplify the investigation by consid-

ering only the one-group neutron transport equation rather than the full radiative transfer equations, which include a material temperature equation as well as the radiation transport equation. The vast majority of relevant properties of a VEF method for radiative transfer can be tested with an analogous method for one-group neutron transport. Furthermore, a high-order DG-MFEM VEF method could be of interest for neutronics in addition to radiative transfer calculations. A full investigation for radiative transfer calculations will be carried out in a future study.

The remainder of this paper is organized as follows. First, we describe the VEF method analytically. Then we describe our discretized  $S_N$  equations, followed by a description of the discretized VEF drift-diffusion equation. We next give computational results. More specifically, we describe two ways to represent the  $S_N$  variable Eddington factor in the MFEM drift-diffusion equation and several ways to construct the  $S_N$  scattering source from the drift-diffusion solution for the scalar flux. Each of these options yields a different VEF method. The accuracy of these methods is then compared to that of the standard LLDG  $S_N$  solution for several test problems, and the iterative convergence rate of these methods is compared to that of the LLDG  $S_N$  equations with fully-consistent  $S_2$ SA acceleration. Finally, we give conclusions and recommendations for future work.

## 2 The VEF Method

### 2.1 The Algorithm

Here, we describe the VEF method for a planar geometry, fixed-source problem:

$$\mu \frac{\partial \psi}{\partial x}(x, \mu) + \sigma_t(x) \psi(x, \mu) = \frac{\sigma_s(x)}{2} \int_{-1}^1 \psi(x, \mu') d\mu' + \frac{Q(x)}{2}, \quad (1)$$

where  $\mu = \cos \theta$  is the cosine of the angle of flight,  $\theta$ , relative to the  $x$ -axis,  $\sigma_t(x)$  and  $\sigma_s(x)$  the total and scattering macroscopic cross sections,  $Q(x)$  the isotropic fixed-source and  $\psi(x, \mu)$  the angular flux. Applying the Discrete Ordinates ( $S_N$ ) angular discretization yields the following set of  $N$  coupled, ordinary differential equations:

$$\mu_n \frac{d\psi_n}{dx}(x) + \sigma_t(x)\psi_n(x) = \frac{\sigma_s(x)}{2}\phi(x) + \frac{Q(x)}{2}, \quad 1 \leq n \leq N, \quad (2)$$

where  $\psi_n(x) = \psi(x, \mu_n)$  is the angular flux in direction  $\mu_n$ . The  $\mu_n$  are stipulated by an  $N$ -point Gauss quadrature rule such that the scalar flux,  $\phi(x)$ , is numerically integrated as follows:

$$\phi(x) = \sum_{n=1}^N w_n \psi_n(x), \quad (3)$$

where  $w_n$  is the quadrature weight corresponding to  $\mu_n$ .

The VEF method begins by solving Eq. 2 while lagging the scattering term. This is called a source iteration, and is represented as follows

$$\mu_n \frac{d\psi_n^{\ell+1/2}}{dx}(x) + \sigma_t(x)\psi_n^{\ell+1/2}(x) = \frac{\sigma_s(x)}{2}\phi^\ell(x) + \frac{Q(x)}{2}, \quad 1 \leq n \leq N, \quad (4)$$

where  $\ell$  is the iteration index. The scalar flux used in the scattering term,  $\phi^\ell$ , is assumed to be known either from the previous iteration or from the initial guess if  $\ell = 0$ . The use of a half-integral index indicates that a source iteration is the first of a two-step iteration scheme. However, if one is only doing Source Iteration (SI) without acceleration, the second step would simply be to set the final scalar flux iterate to the iterate after the source iteration:

$$\phi(x)^{\ell+1} = \phi(x)^{\ell+1/2}. \quad (5)$$

SI is slow to converge in optically thick and highly scattering systems, and this is the motivation for accelerating source iteration using the VEF method. The second iterative step of the VEF method is to obtain a final “accelerated” iterate for the scalar flux by solving the VEF drift-diffusion equation using angular flux shape information from the source iteration step:

$$-\frac{d}{dx} \frac{1}{\sigma_t} \frac{d}{dx} [\langle \mu \rangle^{\ell+1/2} \phi^{\ell+1}] + \sigma_a \phi^{\ell+1} = Q, \quad (6)$$

where the Eddington factor is given by

$$\langle \mu^2 \rangle^{\ell+1/2}(x) = \frac{\int_{-1}^1 \mu^2 \psi^{\ell+1/2}(x, \mu) d\mu}{\int_{-1}^1 \psi^{\ell+1/2}(x, \mu) d\mu}. \quad (7)$$

Note that the Eddington factor depends only upon the angular shape of the angular flux, and not its magnitude. This drift diffusion equation is derived by first taking the first two angular moments of Eq. 2:

$$\frac{d}{dx} J(x) + \sigma_a(x) \phi(x) = Q(x), \quad (8a)$$

$$\frac{d}{dx} [\langle \mu^2 \rangle \phi(x)] + \sigma_t(x) J(x) = 0, \quad (8b)$$

where  $J(x)$  is the current. Then Eq. 8b is solved for  $J(x)$ , and this expression is then substituted into Eq. 8a. Performing a SI, computing the Eddington factor from the SI angular flux iterate, and then solving the drift-diffusion equation to obtain a new scalar flux iterate completes one accelerated iteration. These iterations are repeated until convergence of the scalar flux is achieved.

Acceleration occurs because the angular shape of the angular flux, and thus the Eddington factor, converges much faster than the scalar flux. In addition, the solution of the drift-diffusion equation includes scattering. This inclusion compensates for lagging the scattering

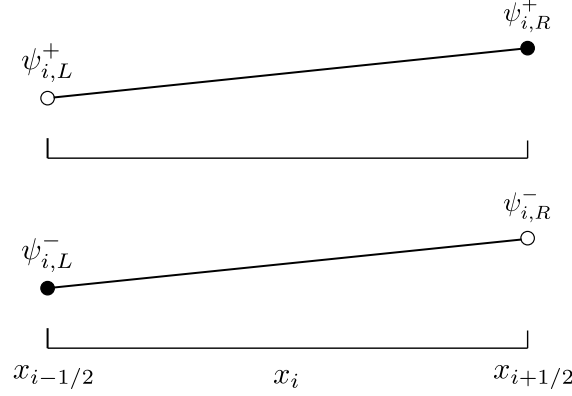


Figure 1: The distribution of unknowns in an LLDG cell. The superscript  $+$  and  $-$  indicate the angular fluxes for  $\mu_n > 0$  and  $\mu_n < 0$ , respectively.

term in the SI step.

The VEF method allows the  $S_N$  equations and drift diffusion equations to be solved with arbitrarily different spatial discretization methods. The following sections present the application of the Lumped Linear-Discontinuous Galerkin (LLDG) spatial discretization to the  $S_N$  equations and the Mixed Finite-Element Method (MFEM) to the VEF drift-diffusion equation.

## 2.2 Lumped Linear Discontinuous Galerkin $S_N$

The spatial grid and distribution of unknowns for an LLDG cell are shown in Fig. 1. We assume a computational domain of length  $x_b$  discretized into  $I$  cells. The cell centers are integral and the cell edges are half integral. The two unknowns in each cell for each discrete angle are the left and right edge discontinuous angular fluxes,  $\psi_{n,i,L}^{\ell+1/2}$  and  $\psi_{n,i,R}^{\ell+1/2}$ .

The LLDG discretization of Eq. 4 is then:

$$\mu_n \left( \psi_{n,i}^{\ell+1/2} - \psi_{n,i-1/2}^{\ell+1/2} \right) + \frac{\sigma_{t,i} h_i}{2} \psi_{n,i,L}^{\ell+1/2} = \frac{\sigma_{s,i} h_i}{4} \phi_{i,L}^{\ell} + \frac{h_i}{4} Q_{i,L}, \quad (9a)$$

$$\mu_n \left( \psi_{n,i+1/2}^{\ell+1/2} - \psi_{n,i}^{\ell+1/2} \right) + \frac{\sigma_{t,i} h_i}{2} \psi_{n,i,R}^{\ell+1/2} = \frac{\sigma_{s,i} h_i}{4} \phi_{i,R}^{\ell} + \frac{h_i}{4} Q_{i,R}, \quad (9b)$$

where  $h_i$ ,  $\sigma_{t,i}$ ,  $\sigma_{s,i}$ , and  $Q_{i,L/R}$  are the cell width, total cross section, scattering cross section and discontinuous fixed source in cell  $i$ . The discontinuous scalar fluxes,  $\phi_{i,L/R}^{\ell}$ , are assumed to be known from the previous iteration or the initial guess when  $\ell = 0$ . The cell edged angular fluxes are uniquely defined by upwinding:

$$\psi_{n,i-1/2}^{\ell+1/2} = \begin{cases} \psi_{n,i-1,R}^{\ell+1/2}, & \mu_n > 0 \\ \psi_{n,i,L}^{\ell+1/2}, & \mu_n < 0 \end{cases}, \quad (10a)$$

$$\psi_{n,i+1/2}^{\ell+1/2} = \begin{cases} \psi_{n,i,R}^{\ell+1/2}, & \mu_n > 0 \\ \psi_{n,i+1,L}^{\ell+1/2}, & \mu_n < 0 \end{cases}. \quad (10b)$$

The cell centered angular flux is the average of the left and right discontinuous edge fluxes:

$$\psi_{n,i}^{\ell+1/2} = \frac{1}{2} \left( \psi_{n,i,L}^{\ell+1/2} + \psi_{n,i,R}^{\ell+1/2} \right). \quad (11)$$

Equations 9a, 9b, 10a, 10b, and 11 can be combined and rewritten as

$$\begin{bmatrix} \mu_n + \sigma_{t,i} h_i & \mu_n \\ -\mu_n & \sigma_{t,i} + \mu_n \end{bmatrix} \begin{bmatrix} \psi_{n,i,L}^{\ell+1/2} \\ \psi_{n,i,R}^{\ell+1/2} \end{bmatrix} = \begin{bmatrix} \frac{\sigma_{s,i} h_i}{2} \phi_{i,L}^{\ell} + \frac{h_i}{2} Q_{i,L} + 2\mu_n \psi_{n,i-1,R}^{\ell+1/2} \\ \frac{\sigma_{s,i} h_i}{2} \phi_{i,R}^{\ell} + \frac{h_i}{2} Q_{i,R} \end{bmatrix}, \quad (12)$$

for sweeping from left to right ( $\mu_n > 0$ ) and

$$\begin{bmatrix} -\mu_n + \sigma_{t,i} h_i & \mu_n \\ -\mu_n & -\mu_n + \sigma_{t,i} h_i \end{bmatrix} \begin{bmatrix} \psi_{n,i,L}^{\ell+1/2} \\ \psi_{n,i,R}^{\ell+1/2} \end{bmatrix} = \begin{bmatrix} \frac{\sigma_{s,i} h_i}{2} \phi_{i,L}^{\ell} + \frac{h_i}{2} Q_{i,L} \\ \frac{\sigma_{s,i} h_i}{2} \phi_{i,R}^{\ell} + \frac{h_i}{2} Q_{i,R} - 2\mu_n \psi_{n,i+1,L}^{\ell+1/2} \end{bmatrix}, \quad (13)$$



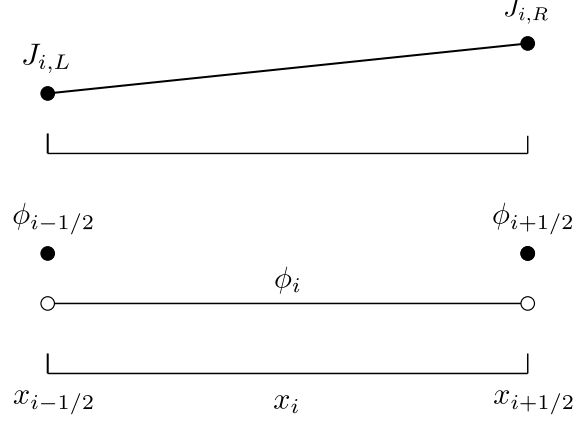


Figure 2: The distribution of unknowns in cell  $i$  for MFEM.

for sweeping from right to left ( $\mu_n < 0$ ), respectively. The right hand sides of Eqs. 12 and 13 are known as the scalar flux from the previous iteration, the fixed source, and the angular flux entering from the downwind cell are all known. By supplying the flux entering the left side of the first cell, the solution for ( $\mu_m > 0$ ) can be propagated from left to right by solving Eq. 12. Similarly, supplying the incident flux on the right boundary allows the solution for ( $\mu_n < 0$ ) to be propagated from right to left with Eq. 13. The cell edge and cell centered Eddington factors needed in the VEF acceleration step are computed as follows:

$$\langle \mu^2 \rangle_{i(\pm 1/2)}^{\ell+1/2} = \frac{\sum_{n=1}^N \mu_n^2 \psi_{n,i(\pm 1/2)}^{\ell+1/2} w_n}{\sum_{n=1}^N \psi_{n,i(\pm 1/2)}^{\ell+1/2} w_n}, \quad (14)$$

where the  $\psi_{n,i\pm 1/2}^{\ell+1/2}$  are defined by Eqs. 10a and 10b and  $\psi_{n,i}$  by Eq. 11.

### 2.3 Mixed Finite-Element Method for VEF Equation

We apply the MFEM method to Eqs. 8a and 8b, and then eliminate the currents to obtain a discretization for Eq. 6. In this method, different basis functions are used for each of the two variables. The unknowns in an MFEM cell are depicted in Fig. 2. The scalar flux is

constant within the cell with discontinuous jumps at the cell edges and the current is a linear function defined by:

$$J_i(x) = J_{i,L}B_{i,L}(x) + J_{i,R}B_{i,R}(x), \quad (15)$$

where  $J_{i,L/R}$  are the currents at the left and right edges of the cell and

$$B_{i,L}(x) = \begin{cases} \frac{x_{i+1/2}-x}{h_i}, & x \in [x_{i-1/2}, x_{i+1/2}] \\ 0, & \text{otherwise} \end{cases}, \quad (16a)$$

$$B_{i,R}(x) = \begin{cases} \frac{x-x_{i-1/2}}{h_i}, & x \in [x_{i-1/2}, x_{i+1/2}] \\ 0, & \text{otherwise} \end{cases}, \quad (16b)$$

are the MFEM basis functions. The constant-linear MFEM yields second order accuracy for both the scalar flux and the current. The spatial grid used in this step is identical to the grid used in the LLDG  $S_N$  step.

The MFEM representation yields five unknowns per cell:  $\phi_{i-1/2}$ ,  $\phi_i$ ,  $\phi_{i+1/2}$ ,  $J_{i,L}$ , and  $J_{i,R}$ . However, each edge flux on the mesh interior is shared by two cells, so with  $I$  cells there are  $I$  cell-center scalar fluxes,  $2I$  currents, and  $2I - 1$  interior-mesh cell-edge scalar fluxes, and 2 boundary cell-edge scalar fluxes. An equation for  $\phi_i$  is found by integrating Eq. 8a over cell  $i$ :

$$J_{i,R} - J_{i,L} + \sigma_{a,i}h_i\phi_i = Q_ih_i, \quad (17)$$

where  $\sigma_{a,i}$  and  $Q_i$  are the absorption cross section and source in cell  $i$ . Equations for  $J_{i,L/R}$  are found by multiplying Eq. 8b by  $B_{i,L/R}$  and integrating over cell  $i$ :

$$-\langle\mu^2\rangle_{i-1/2}\phi_{i-1/2} + \langle\mu^2\rangle_i\phi_i + \sigma_{t,i}h_i\left(\frac{1}{3}J_{i,L} + \frac{1}{6}J_{i,R}\right) = 0, \quad (18a)$$

$$\langle \mu^2 \rangle_{i+1/2} \phi_{i+1/2} - \langle \mu^2 \rangle_i \phi_i + \sigma_{t,i} h_i \left( \frac{1}{6} J_{i,L} + \frac{1}{3} J_{i,R} \right) = 0, \quad (18b)$$

where the fixed source has been assumed to be isotropic. The Eddington factors,  $\langle \mu^2 \rangle_{i(\pm 1/2)}$ , are computed with Eq. 14 using the angular fluxes from the LLDG  $S_N$  step. Eliminating  $J_{i,R}$  from Eq. 18a and  $J_{i,L}$  from Eq. 18b yields:

$$J_{i,L} = \frac{-2}{\sigma_{t,i} h_i} \left\{ 2 [\langle \mu^2 \rangle_i \phi_i - \langle \mu^2 \rangle_{i-1/2} \phi_{i-1/2}] - [\langle \mu^2 \rangle_{i+1/2} \phi_{i+1/2} - \langle \mu^2 \rangle_i \phi_i] \right\}, \quad (19a)$$

$$J_{i,R} = \frac{-2}{\sigma_{t,i} h_i} \left\{ 2 [\langle \mu^2 \rangle_{i+1/2} \phi_{i+1/2} - \langle \mu^2 \rangle_i \phi_i] - [\langle \mu^2 \rangle_i \phi_i - \langle \mu^2 \rangle_{i-1/2} \phi_{i-1/2}] \right\}. \quad (19b)$$

An equation for  $\phi_{i+1/2}$  on the mesh interior is found by enforcing continuity of current at the cell edges:

$$J_{i,R} = J_{i+1,L}. \quad (20)$$

Using the definitions of  $J_{i,L}$  and  $J_{i,R}$  from Eqs. 19a and 19b in the balance equation (Eq. 17) and continuity equation (Eq. 20) yields equations for all cell-center fluxes and interior-mesh cell-edge fluxes. The resulting balance and continuity equations are:

$$-\frac{6}{\sigma_{t,i} h_i} \langle \mu^2 \rangle_{i-1/2} \phi_{i-1/2} + \left( \frac{12}{\sigma_{t,i} h_i} \langle \mu^2 \rangle_i + \sigma_{a,i} h_i \right) \phi_i - \frac{6}{\sigma_{t,i} h_i} \langle \mu^2 \rangle_{i+1/2} \phi_{i+1/2} = Q_i h_i, \quad (21a)$$

$$\begin{aligned} -\frac{2}{\sigma_{t,i} h_i} \langle \mu^2 \rangle_{i-1/2} \phi_{i-1/2} + \frac{6}{\sigma_{t,i} h_i} \langle \mu^2 \rangle_i \phi_i - 4 \left( \frac{1}{\sigma_{t,i} h_i} + \frac{1}{\sigma_{t,i+1} h_{i+1}} \right) \langle \mu^2 \rangle_{i+1/2} \phi_{i+1/2} \\ + \frac{6}{\sigma_{t,i+1} h_{i+1}} \langle \mu^2 \rangle_{i+1} \phi_{i+1} - \frac{2}{\sigma_{t,i+1} h_{i+1}} \langle \mu^2 \rangle_{i+3/2} \phi_{i+3/2} = 0. \end{aligned} \quad (21b)$$

The equations for the outer boundary fluxes,  $\phi_{1/2}$  and  $\phi_{I+1/2}$ , involve boundary conditions

together with continuity conditions. For instance, the equation for  $\phi_{1/2}$  is

$$J_{1,L} = J_{1/2} , \quad (22)$$

where  $J_{1,L}$  is defined in Eq. 19a, and  $J_{1/2}$  is the left boundary current defined by a boundary condition. For a reflective condition,

$$J_{1/2} = 0 . \quad (23)$$

For a source condition,

$$J_{1/2} = 2 \sum_{\mu_n > 0} \mu_n \psi_{n,1/2} w_n - B_{1/2} \phi_{1/2} , \quad (24)$$

where

$$B_{1/2} = \frac{\sum_{n=1}^N |\mu_n| \psi_{n,1/2} w_n}{\sum_{n=1}^N \psi_{n,1/2} w_n} \quad (25)$$

is the boundary Eddington factor [9]. The equation for  $\phi_{I+1/2}$  is

$$J_{I,R} = J_{I+1/2} . \quad (26)$$

where  $J_{I,R}$  is defined in Eq. 19b, and  $J_{I+1/2}$  is the right boundary current. For a reflective condition,

$$J_{I+1/2} = 0 . \quad (27)$$

For a source condition,

$$J_{I+1/2} = B_{I+1/2} \phi_{I+1/2} - 2 \sum_{\mu_n < 0} |\mu_n| \psi_{n,I+1/2} w_n , \quad (28)$$

where

$$B_{I+1/2} = \frac{\sum_{n=1}^N |\mu_n| \psi_{n,I+1/2} w_n}{\sum_{n=1}^N \psi_{n,I+1/2} w_n}. \quad (29)$$

These transport-consistent, Marshak-like source boundary conditions are derived starting with the identity

$$J = j^+ - j^-, \quad (30)$$

where  $j^\pm$  denotes the positive half-range currents associated with  $\mu > 0$  and  $\mu < 0$ , respectively. For the left boundary condition, we simply perform the following algebraic manipulations:

$$J = j^+ - j^- = 2j^+ - (j^+ + j^-) = 2j^+ - \frac{j^+ + j^-}{\phi} \phi. \quad (31)$$

For the right boundary condition, we similarly obtain

$$J = j^+ - j^- = (j^+ + j^-) - 2j^- = \frac{j^+ + j^-}{\phi} \phi - 2j^-. \quad (32)$$

Note that these source boundary conditions become equivalent to the standard Marshak boundary conditions if the  $S_N$  angular flux is isotropic. The system of  $2I + 1$  equations for the cell-center and cell-edge fluxes can be assembled into a matrix of both cell-centered and cell-edge scalar fluxes and solved with a banded matrix solver of bandwidth five.

## 2.4 Increased Consistency Between LLDG and MFEM

The  $S_N$  solution provides the drift-diffusion equation with the variable Eddington factor, and the drift-diffusion solution provides the  $S_N$  equations with the scalar flux used to construct the scattering term. One can simply assume a constant dependence for the variable Eddington factor within each cell, as defined in Eq. 14. However, the LLDG discretization

provides the following form for the variable Eddington factor on the interior of each mesh cell:

$$\langle \mu^2 \rangle_i(x) = \frac{\sum_{n=1}^N \mu_n^2 [\psi_{n,i,L} B_{i,L}(x) + \psi_{n,i,R} B_{i,R}(x)]}{B_{i,L}(x) \sum_{n=1}^N w_n \psi_{n,i,L} + B_{i,R}(x) \sum_{n=1}^N w_n \psi_{n,i,R}}. \quad (33)$$

Here, the LLDG angular flux has been represented as a linear function of the MFEM basis functions. Equation 33 is a rational polynomial and cannot be integrated analytically. In this case, two point Gauss quadrature was used to numerically perform the MFEM integrations associated with Eq. 33. The Gauss quadrature points in cell  $i$  are given by

$$x_{i,L/R}^G = \frac{h_i}{2} \mp \frac{x_{i+1/2} + x_{i-1/2}}{2\sqrt{3}}, \quad (34)$$

and each quadrature weight is equal to  $h/2$ . This method will be referred to as the rational polynomial representation of the Eddington factor. It is clearly a more accurate representation than a constant representation, and thus is expected to generally yield better drift-diffusion solutions for the scalar flux.

The MFEM representation for the scalar flux is constant within a cell, but the LLDG representation for the scalar flux is linear. This suggests improved accuracy  $S_N$  solution could be achieved by somehow constructing a linear scalar flux dependence from the MFEM solution. One simple method for doing this is to use the MFEM cell-edge scalar fluxes to compute a slope. This works quite well, for neutronics. However, it will be inadequate in a radiative transfer calculation because slopes must also be generated for the material temperatures, and an MFEM approximation for the temperatures will not include edge temperatures. We have chosen to use a more generally applicable approach based upon standard data reconstruction techniques that require only cell-centered values to compute slopes [10]. We also limit such slopes to avoid non-physical scalar fluxes. For example, the

reconstructed left and right scalar fluxes in a cell  $i$  are given by

$$\phi_{i,L/R} = \phi_i \mp \frac{1}{4}\xi_i (\Delta\phi_{i+1/2} + \Delta\phi_{i-1/2}) , \quad (35)$$

where  $\xi$  is a van Leer-type slope limiter [10]:

$$\xi_i = \begin{bmatrix} 0, & \text{if } r_i \leq 0, \\ \max \left\{ \frac{r_i}{1+r_i}, \frac{1}{1+r_i} \right\}, & \text{if } r_i > 0, \end{bmatrix} \quad (36)$$

$$r_i = \frac{\Delta\phi_{i-1/2}}{\Delta\phi_{i+1/2}} , \quad (37)$$

and

$$\Delta\phi_{i+1/2} = \phi_{i+1} - \phi_i . \quad (38)$$

On the boundaries, we use

$$\phi_{1,L/R} = \phi_1 \mp \frac{1}{2}\Delta\phi_{3/2} , \quad (39a)$$

$$\phi_{I,L/R} = \phi_I \mp \frac{1}{2}\Delta\phi_{I-1/2} . \quad (39b)$$

We also set any negative left or right flux values in the boundary cells to zero by appropriately rotating the slopes. [I'm not sure if this was how the slopes were really calculated, but we need to fully explain what was done, and we should do something to prevent negativities from arising.](#)

### 3 Computational Results

[We need to describe the problem here.](#) Figure 3a shows the iterative convergence as a

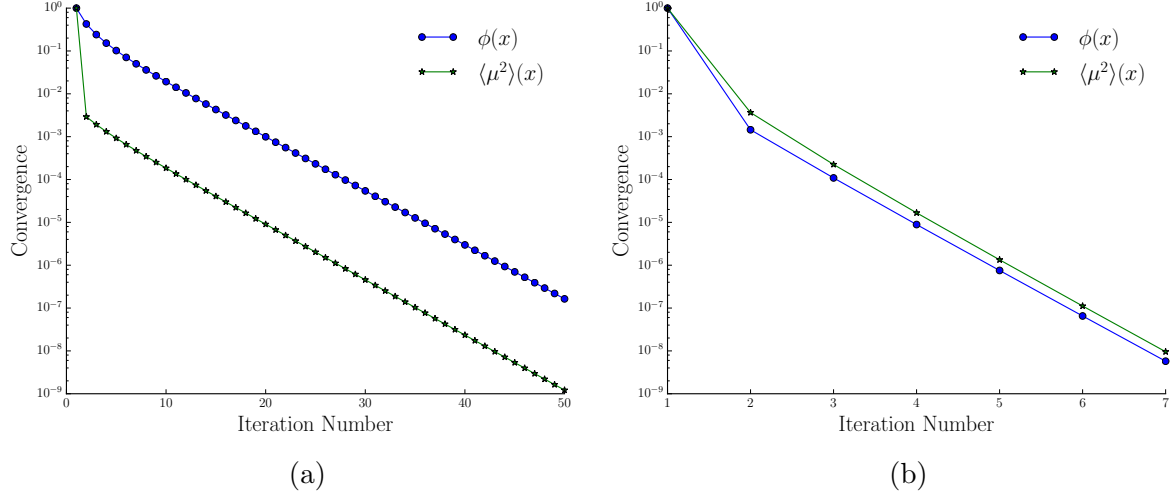


Figure 3: The convergence rate for  $\phi(x)$  and  $\langle \mu^2 \rangle(x)$  for (a) unaccelerated and (b) VEF accelerated SI.

function of unaccelerated iteration number for the scalar flux and the Eddington factor. The Eddington factor's large drop in relative norm [you need to describe the norm](#) between the first and second iterations supports the claim that the angular shape of the angular flux, and thus the Eddington factor, converges rapidly. When compared to Fig. 3b, a plot of the iterative convergence for the VEF method, it is clear that the VEF method transfers the fast rate of convergence of the Eddington factor to the scalar flux.

To compare SI, VEF, and consistently differenced  $S_2SA$ , a homogeneous test problem with a reflecting left boundary, a vacuum right boundary, and a total thickness of 10 cm, was used. This system was discretized into 50 spatial cells. The total macroscopic cross section,  $\sigma_t$ , was set to  $1 \text{ cm}^{-1}$  leading to an optical thickness per cell of 0.2 mfp and a problem thickness of 10 mfp. The convergence tolerance was set to  $10^{-6}$ . [We need to explain the convergence tolerance in full detail.](#) Figure 4 shows the number of iterations required for convergence for SI, VEF, and  $S_2SA$  for varying ratios of  $\sigma_s$  to  $\sigma_t$ . The ratio of unaccelerated to VEF



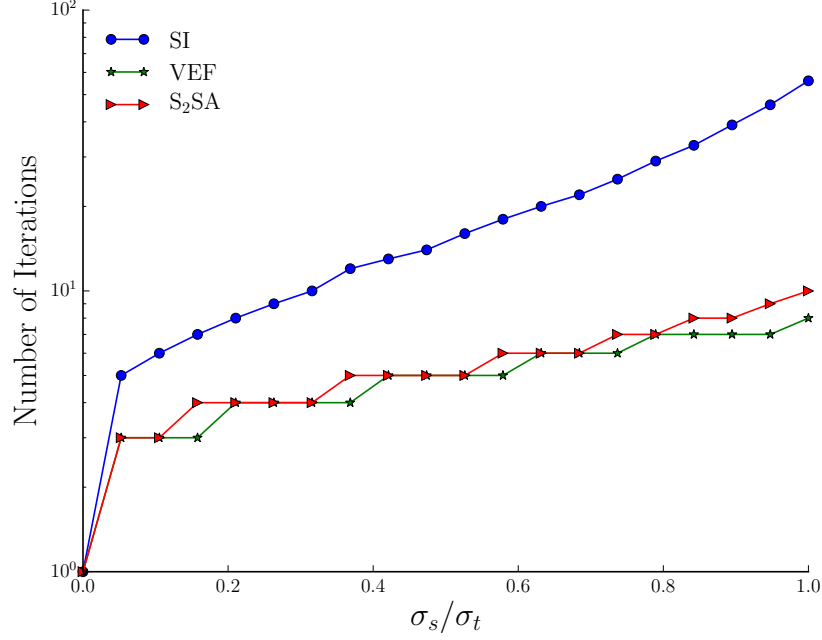


Figure 4: A comparison of the number of iterations required for Source Iteration, VEF acceleration, and S<sub>2</sub>SA to converge for varying ratios of  $\sigma_s$  to  $\sigma_t$ .

accelerated iterations ranged from 1.6 to 7. This suggests that acceleration is occurring and that the VEF method is not just doing twice the amount of work per iteration. In addition, the VEF method performed similarly to S<sub>2</sub>SA. I am skeptical of the numbers for the unaccelerated case. You need to include an estimate of the spectral radius to properly converge the error when the spectral radius is near one. You need a tighter tolerance -  $\text{tol} = \text{tol} * (1 - \rho)$ , where  $\rho$  is the spectral radius estimate. Otherwise you will not actually converge the error to  $\text{tol}$  but to a  $\text{tol}/(1 - \rho)$ .

The Method of Manufactured Solutions (MMS) was used to compare the accuracy of the VEF method as the cell width was decreased. You need to explain how you constructed the MMS solution. I can't tell anything about the problem. In general, you are supposed to provide enough information for the reader to reproduce your calculations. The L2 norm of the

Reconstruction Method	Eddington Representation	Order	$C$	$R^2$
None	Average	1.997	0.682	$9.9999 \times 10^{-1}$
None	Rational Polynomial	1.998	0.687	1.0000
Center	Average	2.007	0.726	$9.9992 \times 10^{-1}$
Center	Rational Polynomial	2.009	0.732	$9.9991 \times 10^{-1}$

Table 1: The order of accuracy, error, and  $R^2$  values for the permutations of the two Eddington representation methods and two slope reconstruction methods.

difference between the numerical and MMS solutions was compared at five logarithmically spaced cell widths between 0.5 mm and 0.01 mm. A line of best fit of the form

$$E = Ch^n \quad (40)$$

was used to find the order of accuracy,  $n$ , and the constant of proportionality,  $C$ , of the numerical error,  $E$ . These values are provided in Table 1 for the permutations of average and rational polynomial Eddington representation and slope reconstruction and no reconstruction. All of the permutations are second order accurate and have similar overall accuracy. This suggests that slope reconstruction and Eddington representation do not affect the *order* of numerical accuracy.

The convergence between unaccelerated SI and the VEF method was compared as a function of cell width for a simple homogeneous slab and for Reed’s problem. In both cases, the left boundary was reflecting and the right boundary was vacuum. The homogeneous slab had a scattering ratio of 0.75. The cross sections and source for Reed’s problem are provided in Table 2. The L2 norm of the difference between the SI solution and VEF solution is plotted for the four permutations of no reconstruction, van Leer slope limited reconstruction, average Eddington representation, and rational polynomial Eddington representation in Figures 5a and 5b for the homogeneous slab problem and Reed’s problem.

	Region 1	Region 2	Region 3	Region 4	Region 5
$q$	10	0	0	0	1
$\sigma_t$	10	0.001	1	5	1
$\sigma_a$	10	0	0.1	0	0.1
Domain	$0 \leq x < 2$	$2 \leq x < 4$	$4 \leq x < 6$	$6 \leq x < 7$	$7 \leq x \leq 8$

Table 2: The cross sections and source used for Reed’s problem.

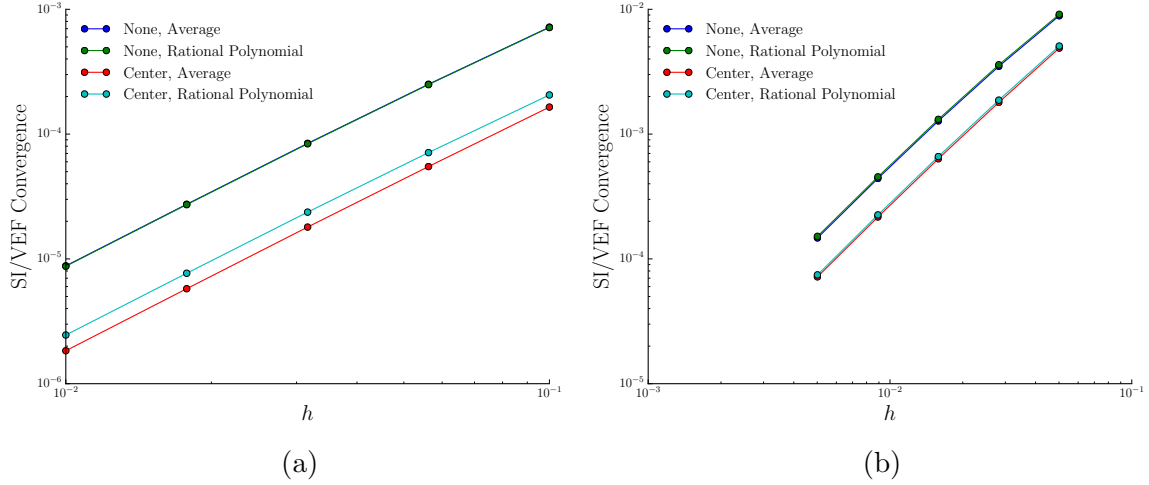


Figure 5: The L2 norm of the difference between SI and the four permutations of the VEF method as the cell spacing is decreased for (a) the homogeneous slab problem and (b) Reed’s problem.

In the homogeneous problem, VEF with van Leer limited slope reconstruction was five times more convergent than VEF without reconstruction. Use of the rational polynomial Eddington representation decreased the van Leer reconstruction convergence by 30%. *Wow, I don’t get this. We are allowing the VEF to vary spatially within a cell and getting a less accurate solution.* In Reed’s problem, reconstruction was twice as convergent as no reconstruction. The rational polynomial Eddington representation was 4% less convergent than the average representation. *How did you compute the average value for the VEF? Actually average the space-dependent value of the VEF via Gauss Quadrature, or just evaluate the*

VEF at the center of the cell? We should explain this.

Lastly, slope reconstruction and Eddington representation were tested in the diffusion limit. The cross sections and source were scaled as follows [11]:

$$\sigma_t(x) \rightarrow \sigma_t(x)/\epsilon, \quad (41a)$$

$$\sigma_s(x) \rightarrow \epsilon\sigma_s(x), \quad (41b)$$

$$Q(x) \rightarrow \epsilon Q(x). \quad (41c)$$

As  $\epsilon \rightarrow 0$ , the system becomes diffusive. The number of iterations for convergence within a tolerance of  $10^{-8}$  as  $\epsilon \rightarrow 0$  is plotted in Fig. 6. The error between the VEF solution and the exact diffusion solution is provided in Fig. 7. This supports the claim that the VEF method is robust as all four permutations properly preserved the diffusion limit.

## 4 Conclusions and Future Work

We have presented the VEF method for one-group neutron transport in slab geometry and the pairing of Lumped Linear Discontinuous Galerkin for the  $S_N$  transport step and the constant-linear Mixed Finite-Element Method for the drift diffusion acceleration step. We have numerically demonstrated that the LLDG/MFEM VEF method accelerates Source Iteration by transferring the rapid convergence of the angular shape of the angular flux to the scalar flux. In addition, the VEF method performed similarly to consistently differenced  $S_2SA$ .

Methods for increased consistency between LLDG and MFEM were also presented. This included a more consistent method for computing the Eddington factor on the cell centers

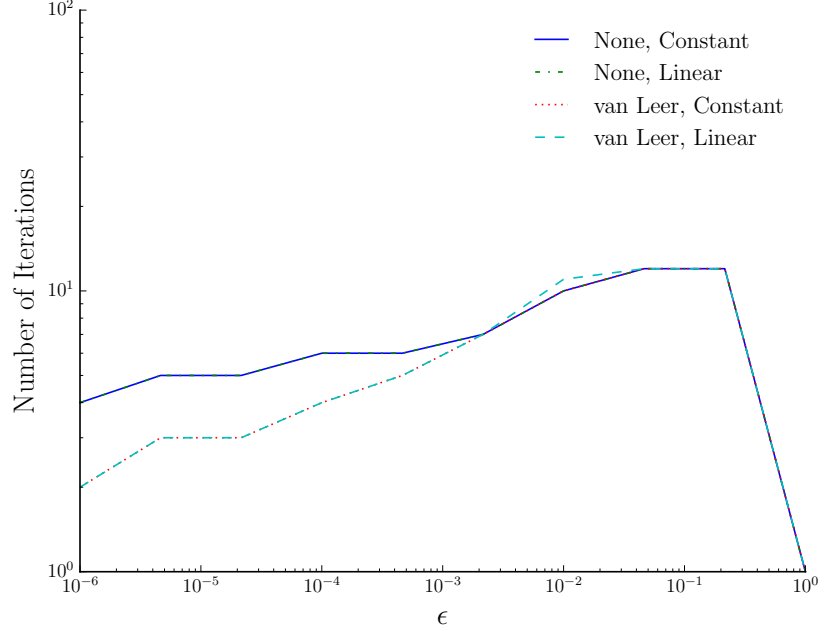


Figure 6: The number of iterations required for convergence for the permutations of slope reconstruction and angular flux representation in the diffusion limit.

and a cell-centered slope reconstruction. It was shown that both the VEF method without and without added consistency measures was second-order accurate as expected from the orders of accuracy of LLDG and MFEM in isolation and that all of the VEF methods were robust in the diffusion limit. In addition, while this nonlinear scheme produces two solutions, one from  $S_N$  and one from drift diffusion, the solutions were shown to converge as the mesh was refined for both homogeneous and inhomogeneous systems. Furthermore, the drift-diffusion solution for scalar flux and current is conservative and thus is the preferred solution to compute quantities of interest.

Slope reconstruction significantly increased the convergence between the  $S_N$  and drift diffusion solutions. While consistent representation of the Eddington factor did not significantly impact numerical accuracy or solution convergence, it is expected to be important

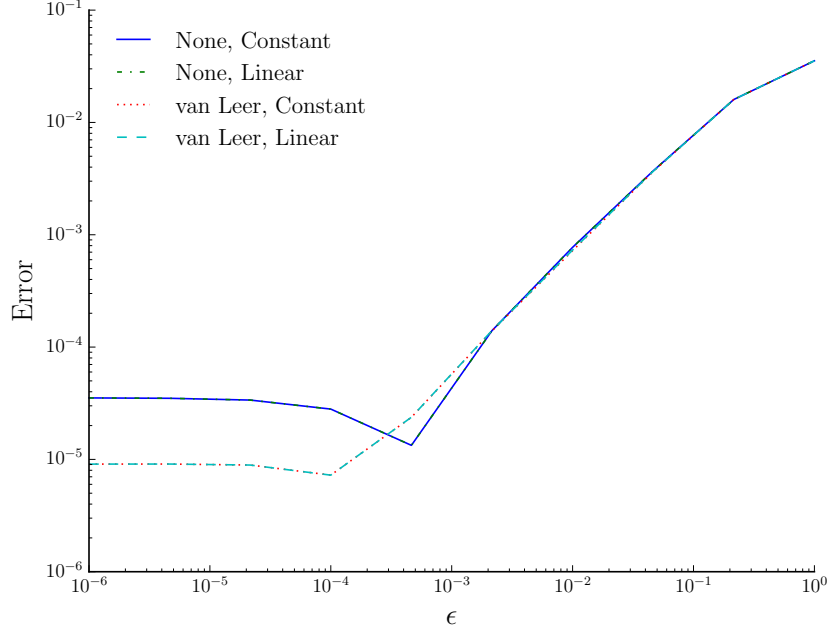


Figure 7: The error between the VEF methods and the exact diffusion solution as  $\epsilon \rightarrow 0$ .

in radiative transfer calculations due to the non-linearities in temperature and the spatial dependence of the cross sections. We need to take a look at this. I want to make sure I understood what you did. I don't understand why we see less accuracy with the rational polynomial representation.

The VEF method is especially suited for multiphysics calculations as VEF drift diffusion is conservative and much less expensive than a transport sweep. In addition, the multiphysics and transport discretizations can be arbitrarily different.

Future work includes extending the VEF method presented in this paper to the radiative transfer equations, verifying the VEF method in higher dimensions, and generalizing the method to higher order finite-elements.

## References

- [1] M.L. Adams and E.W. Larsen. Fast iterative methods for discrete-ordinates particle transport calculations. *Progress in Nuclear Energy*, 40(1):3–159, 2002.
- [2] R.E. Alcouffe. Diffusion synthetic acceleration methods for the diamond-differenced discrete-ordinates equations. *Nuclear Science and Engineering*, 64:344–355, 1977.
- [3] J.S. Warsa, T.A. Wareing, and J.E. Morel. Fully-consistent diffusion-synthetic acceleration of linear discontinuous  $s_n$  transport discretizations on unstructured tetrahedral meshes. *Nuclear Science and Engineering*, 141:235–251, 2002.
- [4] J.E. Morel and E.W. Larsen. A multiple balance approach for differencing the  $s_n$  equations. *Nuclear Science and Engineering*, 105:1–15, 1990.
- [5] Marvin L. Adams and William R. Martin. Diffusion synthetic acceleration of discontinuous finite element transport iterations. *Nuclear Science and Engineering*, 111:145–167, 1992.
- [6] Yaqi Wang and Jean C. Ragusa. Diffusion synthetic acceleration for high-order discontinuous finite element  $s_n$  transport schemes and application to locally refined unstructured meshes. *Nuclear Science and Engineering*, 166(2):145–166, 2010.
- [7] Edward W. Larsen, J.E. Morel, and Warren F. Miller, Jr. Asymptotic solutions of numerical transport problems in optically thick, diffusive regimes. *Journal of Computational Physics*, 69:283–324, 1987.

- [8] V. Dobrev, Tz. Kolev, and R. Rieben. High-order curvilinear finite element methods for lagrangian hydrodynamics. *SIAM Journal on Scientific Computing*, 34:B606–B641, 2012.
- [9] M.M. Miften and E.W. Larsen. The quasi-diffusion method for solving transport problems in planar and spherical geometries. *Journal of Transport Theory and Statistical Physics*, 22(2-3):165–186, 1992.
- [10] B. van Leer. Towards the ultimate conservative difference scheme I: The quest for monotonicity. *Lecture Notes in Physics*, 18:163–168, 1973.
- [11] Edward W. Larsen, J.E. Morel, and Jr. Warren F. Miller. Asymptotic solutions of numerical transport problems in optically thick, diffusive regimes. *Journal of Computational Physics*, 69:283–324, 1987.